



Rock Triaxial Tests: Global Deformation vs Local Strain Measurements—Implications

A. Perbawa¹ · E. Gramajo¹ · T. Finkbeiner¹ · J. C. Santamarina¹

Received: 6 July 2020 / Accepted: 25 January 2021 / Published online: 5 April 2021
© The Author(s) 2021

Abstract

Accurate stress–strain measurements in triaxial tests are critical to compute reliable mechanical parameters. We focus on compliance at the interfaces between the specimen and endcaps, and test specimens under various triaxial conditions using different instrumentation protocols. The tested materials include aluminum, Eagle Ford shale, Berea sandstone, and Jubaila carbonate. Results obtained following common practice reveal that surface roughness at the specimen–endcap interfaces leads to marked seating effects, affects all cap-to-cap based measurements and hinders ultrasonic energy transmission. In particular, cap-to-cap deformation measurements accentuate hysteretic behavior, magnify biases caused by bending and tilting (triggered by uneven surfaces and misalignment), and affect the estimation of all rock parameters, from stiffness to Biot’s α -parameter. Higher confining pressure diminishes seating effects. Local measurements using specimen-bonded strain gauges are preferred (Note: mounting strain gauges on sleeves is ill-advised). We confirm that elastic moduli derived from wave propagation measurements are higher than quasi-static moduli determined from local strain measurements using specimen-bonded strain gauges, probably due to the lower strain level in wave propagation and preferential high-velocity travel path for first arrivals.

Keywords Strain gauge · LVDT · Triaxial testing · Ultrasonic · Static modulus · Dynamic modulus

1 Introduction

Mechanical parameters such as stiffness, Poisson’s ratio and Biot’s α -parameter are used for analyses and designs in the geotechnical, petroleum, and mining sectors. Inherent biases within triaxial tests can obscure and distort measured values and produce unrepresentative rock properties.

Current best practice involves strain measurements conducted mid-height using strain gauges mounted directly on top of the rock specimen and that extend across at least ten-grain diameters (ASTM International D7012-14 (2014)). However, common practice uses global deformation sensors mounted either on both endcaps across the entire length of the specimen or coupled on top of the jacket to measure deformations within the central zone along with the specimen height. Table 1 lists strain and deformation sensors used in geomechanics laboratories.

Measurements using cap-to-cap deformation sensors include seating effects due to topographic differences at the specimen–endcap interfaces and non-uniform strains along with the specimen due to restrains at the interface (Baldi et al. 1988). Local measurements avoid the impact of unwanted deformations at the specimen–endcap interfaces and result in computed stiffness values between 15% to 45% higher than cap-to-cap measurements (Isah et al. 2018; Yimsiri et al. 2005; Kung 2007; Xu et al. 2014; Xu 2017; Kumar et al. 2016).

In this study, we conduct axial compression tests with cylindrical aluminum and intact-rock specimens. We compare stress–strain plots obtained with local measurements using strain gauges against computed strains from cap-to-cap and local LVDTs deformation measurements. The study includes high-resolution surface roughness measurements and ultrasonic velocity data to gain an enhanced understanding of specimen–endcap contact effects. We use these results to quantitatively address seating effects and understand discrepancies in estimated moduli obtained from local and global measurements.

✉ A. Perbawa
andika.perbawa@kaust.edu.sa

¹ King Abdullah University of Science and Technology,
Thuwal, Mecca, Saudi Arabia

Table 1 Overview of strain measurement devices used in published triaxial studies

Strain measurement devices/techniques	Measurement Ranges and Resolutions	Benefits/Limitations	References
Local measurements/techniques			
Strain Gauges	0.3 – 150 mm range Less than 1 μm resolution	-Flexible, submersible, -Requires complete sealing, not reusable, strain drifting, time intensive installation	Howarth (1984), van Heerden (1987)
Local Linear Variable Differential Transformer (LVDT)	Up to 10 mm range Less than 1 μm resolution	-Good resolution, stability, linear calibration, reusable, submersible -Costly, susceptible to jamming, slippage errors	Atkinson (2000), Wild et al. (2017)
Electro Level Inclinometer	Resolution up to 1 μm	-Submersible, compatible with unconsolidated specimens -Bulky, prone to tilting effects, hysteresis effects	Jardine et al. (1984), Symes and Burland (1984)
Hall Effect Local Strain Transducers	4–6 mm range Less than 0.1 μm resolution	-Fixed or floating type -Difficulties in sensor alignment, and sensitive to lower pad rotations	Clayton and Khatrush (1986)
Digital Image Correlation using Digital Camera	Ranges and resolutions dependent on camera specifications	-Straight forward operation -Edge effects, requires clear confining fluid and transparent pressurized vessel	Bhandari et al. (2012), Li et al. (2016)
Local Strain Transducers-LST	Up to 1.5 mm range 1 μm resolution	-Reusable -Non-linear calibration, slippage error due to clamping on the jacket	Tatsuoka (1988)
Proximity Sensors	Up to 5 mm range Up to 10 nm resolution	-Fixed/floating, high resolution -Expensive, complex setup, mostly non-submersible	Hird and Yung (1989)
Fiber Bragg Grating—FBG	Up to 80 mm range. 4.45 μm resolution	-Less expensive than LDT -Bulky, and slippage error due to clamping on the jacket	Xu (2017)
Global measurements/techniques			
Cap-to-cap LVDT	Up to 1 m range Less than 1 μm resolution	-Submersible, easy to install, linear calibration, reusable -Prone to seating and bending effects	Filho (1985), Tisato and Madonna (2012)

2 Experimental Studies

We tested standard aluminum rods and three lithologically different intact-rock specimens prepared from outcrop samples. Experimental details follow.

2.1 Test Protocol

All tests start with a detailed characterization of the specimen and endcaps surfaces using an optical profilometer. The chromatic confocal interferometer has a spot size of $d = 7 \mu\text{m}$ and provides a lateral resolution of $\Delta x \approx 15 \mu\text{m}$ and vertical resolution of 0.2 μm (NANOVEA Jr25). For

comparison, we also gather topographic data using the standard procedure that involves a $d = 1 \text{ mm}$ tip size and elevation data every $\Delta x = 3 \text{ mm}$ separation (ASTM International D4543-08 (2008)).

Then, we mount two strain gauges diametrically opposite to each other at the mid-height of the specimen (installation details in ASTM International D7012-14 (2014)). We use linear or rosette type strain gauges in this study. The rosette gauges have a 3.18 mm length, 4.57 mm grid width, gauge factor of 2.15, resistance of 350 Ω and $a \pm 3 \times 10^{-2}$ strain range; these rosettes allow the simultaneous collection of axial and radial strain data for the accurate determination of Poisson's ratio. The linear strain gauges are 3.18 and 12.7 mm long with $a \pm 3 \times 10^{-2}$ strain range; both linear gauges have a similar gauge width of 4.57 mm, resistance

of 350 Ω, and gauge factor of 2.175. We test two different mounting types: gauges attached directly onto the specimen i.e., beneath the Viton sleeve (Fig. 1a), and gauges bonded onto the Viton sleeve (Fig. 1b). The Viton sleeve has a 0.5 mm thickness, a maximum shrink ratio of 2:1, and a working temperature range from − 55 °C to 200 °C. We also examine two installations for the LVDTs: cap-to-cap (Configuration A and B) and local (Configuration C in Fig. 1).

In addition to the local strain and global deformation measurements, we acquire ultrasonic transit times for all specimens during loading/unloading cycles. The instrumentation involves P-wave crystals and two orthogonally polarized S-wave transducers. At each stress level, we gather and stack 512 signals to enhance the signal-to-noise ratio with minimal preconditioning.

The loading sequence involves (1) three loading/unloading cycles to 40 MPa at different strain rates (Fig. 2); and (2) three loading/unloading cycles to 60 MPa. We repeat the last test at four confining stress levels: 0 MPa (unconfined), 10 MPa, 30 MPa and finally 60 MPa. The selected confining stress levels reflect field conditions encountered in infrastructure and geo-energy applications. Load cycles allow us to investigate the effect of consecutive axial loading/unloading on both seating effects and stiffness, and the relationship between seating effects and axial deviatoric stress.

2.2 Standard Aluminum Specimen

The experimental study starts with a standard aluminum 6061-T6 specimen given its well-known properties (Table 2).

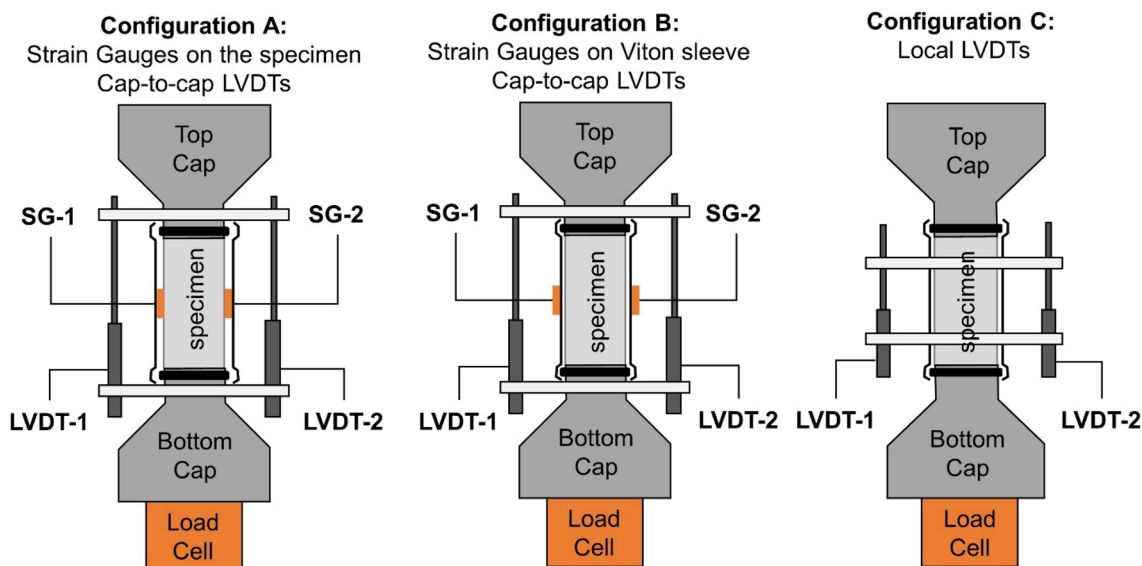


Fig. 1 Instrumentation. Configuration a: two specimen-bonded strain gauges. Configuration b: two strain gauges bonded on top of the Viton sleeve. Configurations a and b: cap-to-cap LVDTs. Configuration c: local LVDTs mounted on top of the Viton sleeve

Fig. 2 Aluminum specimen. **a** Loading history. **b** Stress–strain curves for an unpolished aluminum specimen. Green lines: strain measured with strain gauges. Blue lines: strain computed from cap-to-cap LVDT measurements. Stress–strain curves follow the same loading unloading paths regardless of strain rates. Seating effects readily seen in LVDT data. Dashed black line: standard aluminum Young’s modulus $E = 69$ GPa (Color figure online)

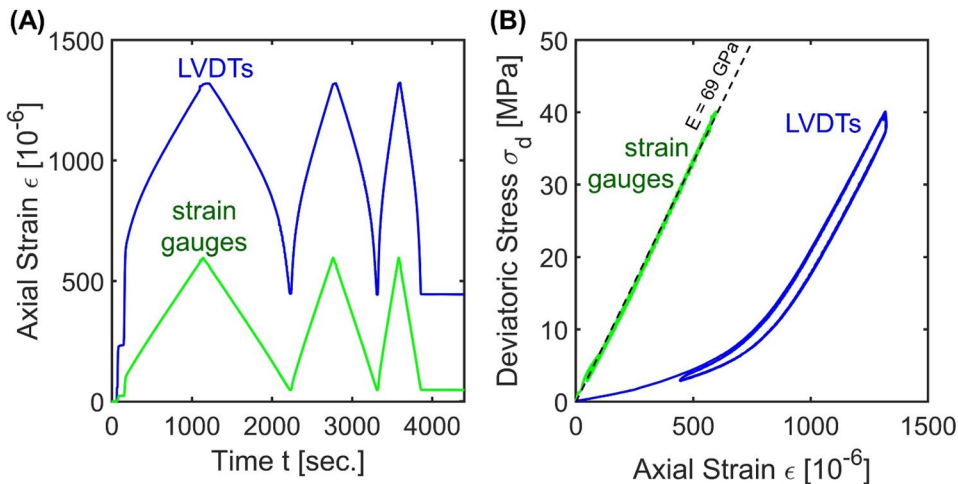


Table 2 Specimen specifications, confining pressures and peak stresses used during the loading/unloading cycles

Specimen	Length [mm] ^b	Diameter [mm] ^b	L:D Ratio	Mass [gr] ^c	Estimated UCS [MPa]	Confining Pressure [MPa]	Peak Stress [MPa]		
							1st cycle	2nd cycle	3rd cycle
Aluminum	50.230	25.105	2.00:1	67.132	310 ^a	0, 10, 30, 60	60	60	60
Eagle Ford Shale	50.896	25.435	2.00:1	65.639	130–150	0	58	58	58
Berea Sandstone	51.349	25.385	2.02:1	55.194	62–78	0	35	35	–
Jubaila Carbonate 1 (Packstone)	57.841	26.813	2.16:1	78.752	24–48	0	21	21	–
Jubaila Carbonate 2 (Wackestone)	53.953	26.714	2.02:1	72.989	24–48	0	10	15	20

Note: all rock specimen come from outcrop samples

^aUCS value for Aluminum 6061-T6 obtained from ASM Handbook (1990). Typical aluminum 6061-T6 composition: 95.8–98.6% Al, 0.04–0.35% Cr, 0.15–0.4% Cu, Max 0.7% Fe, 0.8–12% Mg, Max 0.15% Mn, 0.4–0.8% Si, Max 0.15% Ti, Max 0.25% Zn

^bUncertainty in length and diameter are 5 μm

^cUncertainty in mass is 0.5 mg. The average top and bottom surface roughness for the rock specimens is $\sim 10 \mu\text{m}$

We explore the impact on seating effects by testing (1) the original unpolished specimen, and (2) the specimen after shaving both end surfaces using a precision CNC milling machine (herein called “polished specimen”—ASTM International D4543-08 (2008)). Before testing, we measured surface roughness in both cases using the optical profilometer (detailed above—NANOVEA Jr25).

2.3 Rock Specimens

We extend the experimental study to rock specimens using the same test protocols described above. The selected specimens include lower Eagle Ford shale (Western Gulf outcrop, USA), late Upper Jurassic Jubaila carbonates (Riyadh outcrop, Saudi Arabia), and Berea sandstone (Waverly Group outcrop, USA). The Eagle Ford shale specimen has a bedding angle perpendicular to the specimen’s axis. The Jubaila carbonate specimens have minor stylolite streaks perpendicular to the specimen’s axis. The Berea sandstone is a homogeneous specimen

with 19.9% porosity. Table 2 summarizes specimen properties, peak axial stresses, and applied confining pressures.

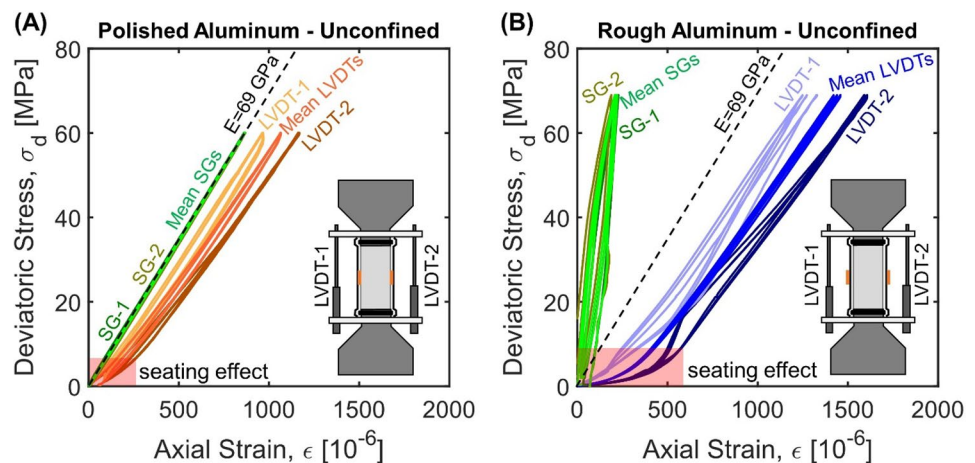
3 Experimental Results

Experimental results obtained with the standard aluminum specimen isolate boundary effects for a well-known homogeneous material. We present these results first, followed by data gathered with rock specimens.

3.1 Local Strain vs. Global Deformation

The stress–strain curves computed using cap-to-cap LVDTs deformation measurements show hysteresis. The computed stiffness $E \approx 59 \text{ GPa}$ is markedly below the reference Young’s modulus for aluminum $E \approx 69 \text{ GPa}$ (ASM Handbook 1990, Fig. 2), and deviations from linearity are more

Fig. 3 Stress–strain response for rough and polished aluminum specimens. Data gathered using cap-to-cap LVDTs and strain gauges SG. **a** Polished specimen with specimen-bonded strain gauges. **b** Rough specimen with strain gauges mounted on top of the Viton sleeve. Green lines: average strain measurements obtained using strain gauges. Orange and blue lines: average strain computed from cap-to-cap LVDT measurements. Pink box: seating effects. Dashed black line: standard aluminum Young’s modulus $E = 69 \text{ GPa}$ (Color figure online)



pronounced at lower axial loads. Both polished and unpolished specimens exhibit seating effects on cap-to-cap LVDTs data, albeit with different degrees (Fig. 3).

Seating effects and hysteresis do not appear on strain data gathered with specimen-bonded strain gauges (Fig. 3a). The measured stiffness agrees with the reference Young’s modulus for aluminum, and strain rates do not affect the measured Young’s modulus ($\dot{\epsilon} = 0.5 \times 10^{-6} \text{ s}^{-1}$, 10^{-6} s^{-1} and $2 \times 10^{-6} \text{ s}^{-1}$ —Fig. 2).

Strains measured from the two diametrically opposite strain gauges plot on top of each other indicating equal strain levels on both sides and, therefore, no specimen bending (Fig. 3). However, deformations measured with the two cap-to-cap LVDTs are different and imply cap tilting. Cap tilting effects are most pronounced in unconfined compression test data, i.e., low initial contact stress.

Local strain and cap-to-cap deformation measurements with rock specimens show similar trends (relevant specimen characteristics listed in Table 2). Seating effects are apparent in all specimens when using cap-to-cap LVDTs deformation measurements (Fig. 4). While there are not seating effects on local measurements gathered with specimen-bonded strain gauges, the Berea sandstone shows an initial non-linear convex response suggesting the presence of microcracks and some grain debonding. The Berea sandstone is a high porosity rock with weak grain-to-grain bonding. In contrast, the Jubaila and Eagle Ford specimens have lower porosity

values with well-cemented matrices; the measured response suggests that these rocks did not experience debonding during sampling and exhumation.

3.2 Instrumentation on the Sleeve—Compliance

Leakage and related experimental difficulties associated with strain gauges affixed to the rock specimen are overcome by mounting instruments on the sleeve (Note: this strategy applies to standard triaxial systems and is avoided in Hoek-cells).

We mounted “local LVDTs” on the specimen mid-height with a separation of 26 mm between clamps (Configuration C, Fig. 1). The local LVDTs data provide stiffness values near the standard Young’s modulus ($E \approx 69 \text{ GPa}$) but exhibit some hysteresis probably due to slippage and compliance effects at the clamp-sleeve-specimen interface (Fig. 5).

Strain gauges mounted on the sleeve show more pronounced compliance issues: the measured strains are markedly smaller than the specimen strains and result in unreasonably high apparent stiffness (Fig. 6b: the estimated Young’s modulus $E \approx 419 \text{ GPa}$ of the light green line is six times higher than the standard value of $E \approx 69 \text{ GPa}$). Higher confining pressures reduce compliance effects (Fig. 6). Nevertheless, mounting strain gauges -even long ones- on top of the sleeve is ill-advised.

Specimen-bonded strain gauges are the best option for pre-peak strain measurements (Figs. 5 and 6). However, strain

Fig. 4 Stress–strain response of intact rock specimens (unconfined and dry). The orange lines correspond to the mean strain values derived from cap-to-cap LVDTs, and the green lines indicate the mean strain values obtained from strain gauges (SG) installed directly onto rock specimens. Strain gauge data lead to higher stiffness

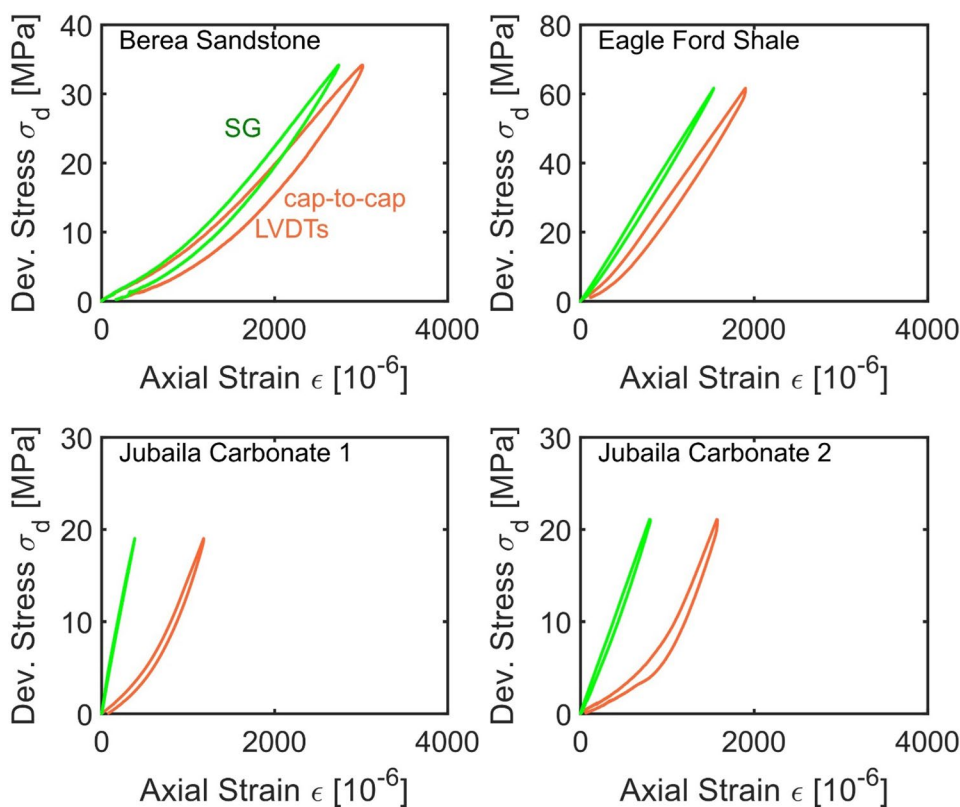


Fig. 5 Stress–strain curves measured for a polished aluminum specimen–LVDT installation effects. Green lines: average strain measured with specimen-bonded strain gauges. Orange and blue lines: average strain computed from cap-to-cap LVDT measurements. Red lines: average strain computed from local LVDTs mounted on the sleeve. Test at 0 MPa (a) and 60 MPa (b) confining pressures. Dashed black line: standard aluminum Young's modulus $E=69$ GPa (Color figure online)

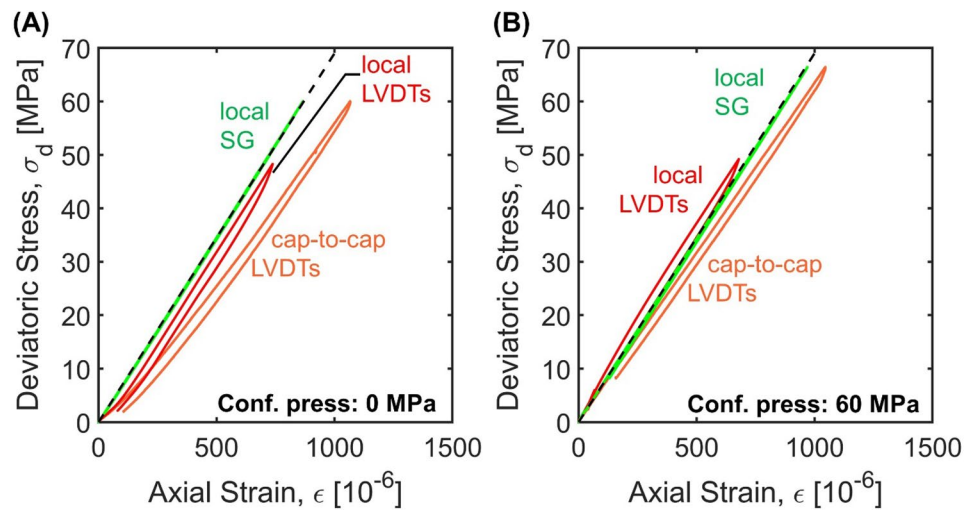
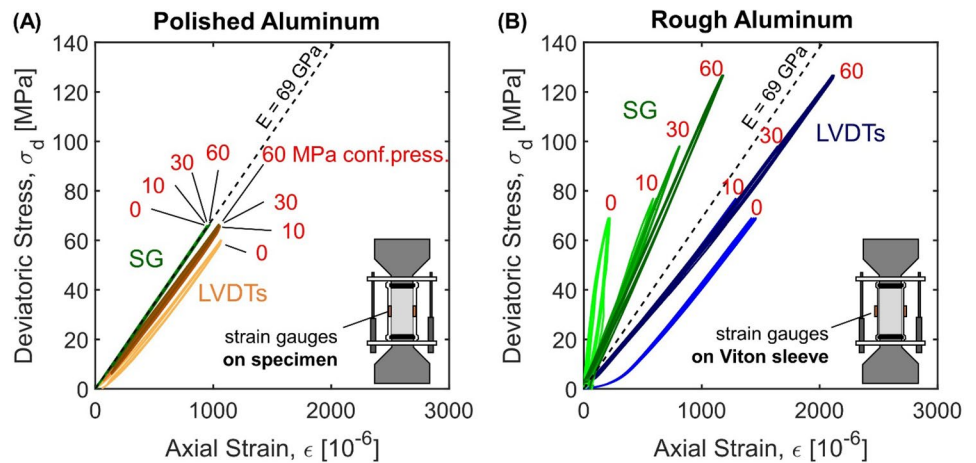


Fig. 6 Stress–strain curves measured for polished and rough aluminum specimens strain gauge installation effects. **a** Polished specimen. **b** Rough specimen. Green lines: average strain measurements with strain gauges mounted on the Viton sleeve. Orange and blue lines: average strain computed from cap-to-cap LVDT measurements. Darker green, blue and orange lines correspond to higher confining pressures. Dashed black line: standard aluminum Young's modulus $E=69$ GPa (Color figure online)



gauges fixed directly on the specimen require properly sealed cables to avoid leakage. In our setup, we pierce a small hole through the Viton sleeve directly at the location where the cables attach to the strain gauges and fill the hole with both silicon sealant and polyurethane. This method is still prone to leaks; one-in-four of our specimens required resealing.

3.3 Surface Roughness

Surface topography gathered with the large $d=1$ mm tip (ASTM International D4543-08 (2008)) renders a smoother surface than the more accurate and higher resolution interferometer data (spot size $d=7$ μm). In fact, the large tip acts as a non-linear low-pass filter (Table 3 see also Fig. 7a–c).

Circumferential profiles gathered at 5 and 10 mm radii on the aluminum specimen end face reveal the effect of polishing on surface topography: the unpolished surfaces have a ~ 150 μm elevation range compared to ~ 38 μm for the

Table 3 Surface roughness for aluminum and rock specimens according to ASTM standard and profilometer measurements

Specimen	ASTM International D4543-08 (2008) (1 mm tip)		Profilometer (7 μm spot size)	
	Max amplitude	Standard deviation	Max amplitude	Standard deviation
	[μm]	[μm]	[μm]	[μm]
Aluminum	23	12	38	13
Eagle Ford shale	11	5	20	6
Jubaila carbonate	10	4	13	4
Berea Sandstone	23	11	41	11
Endcaps	21	11	34	11

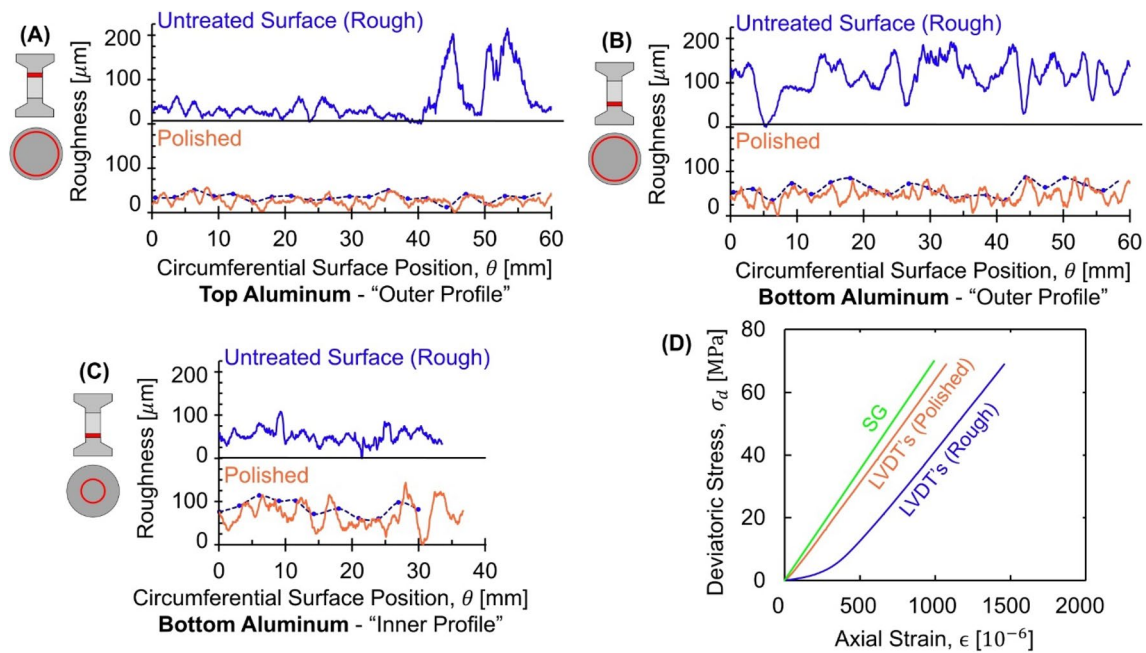


Fig. 7 Surface topography: Polished and rough aluminum specimens. Circumferential profiles of the (a) top and (b and c) bottom surfaces. Optical profilometer: rough surface (blue lines) and polished surface (orange lines). Measurements following ASTM International D4543-08 (2008) standards shown as dashed blue lines. Sketches

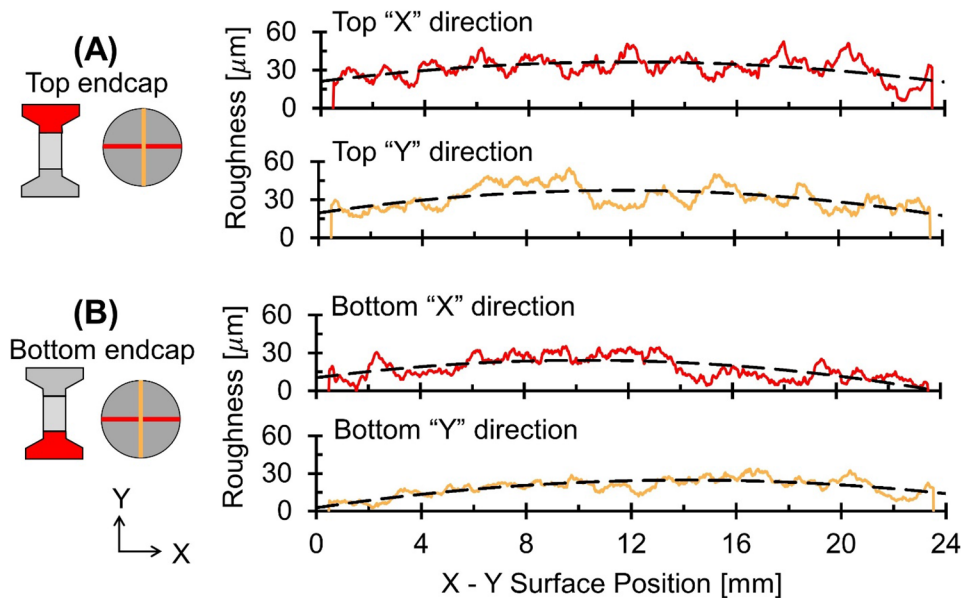
show measurement locations in light red color. **d** Stress–strain curves measured with cap-to-cap LVDTs for the polished (orange) and rough aluminum specimens (blue). The light green line shows specimen-bonded strain gauge measurements (Color figure online)

polished specimen surface (Figs. 7). Note that both values exceed the maximum 25 μm range recommended in ASTM International D4543-08 (2008).

Endcaps have their own topography. Orthogonal radial profiles on the endcaps exhibit a clear concave geometry

with the inner section $\sim 14 \mu\text{m}$ higher than the perimeter (Fig. 8). The following section explores implications on inferred stress–strain data.

Fig. 8 Triaxial endcaps surface profile – Optical profilometer. Top (a) and bottom (b) endcaps. Roughness measurements along two orthogonal paths (see sketches)



4 Analyses and Discussion

4.1 Seating Effects and Surface Roughness

Results in Sect. 3 show that the specimen and endcap topographies are uneven along the perimeter and cause tilting, as hinted by the differential deformation measured with the diametrically opposite cap-to-cap LVDTs. Furthermore, asperities experience stress concentration $\sigma_{asp} = \sigma (A_s/A_{asp})$ where the applied external stress σ is amplified by the area ratio (A_s/A_{asp}) resulting in the localized deformation

$$\delta_{asp} = \epsilon \cdot h = \frac{\sigma_{asp}}{E} h_{asp} = \frac{\sigma}{E} \frac{A_s}{A_{asp}} h_{asp} \tag{1}$$

where subscripts refer to asperities “asp” and specimen “s”. Then, the total strain ϵ_{comp} computed from cap-to-cap LVDTs deformation measurements is

$$\epsilon_{comp} = \frac{\delta_s + 2\delta_{asp}}{h_s + h_{asp}} \approx \frac{\frac{\sigma}{E} h_s + 2 \frac{\sigma}{E} \frac{A_s}{A_{asp}} h_{asp}}{h_s} = \frac{\sigma}{E} \left(1 + 2 \frac{A_s}{A_{asp}} \frac{h_{asp}}{h_s} \right) = \varphi \frac{\sigma}{E} = \varphi_s \tag{2}$$

This first-order approximation captures the main parameters that determine seating effects, herein combined into the single φ -factor. Experimental results show that the φ -factor ranges between $\varphi = 1.7$ and $\varphi = 2.5$ in this study.

Finite element modeling allows us to simulate the complete deformation of the endcap-specimen-endcap stack (COMSOL Multiphysics). The model parameters for elasto-plastic aluminum behavior are elastic modulus $E = 69$ GPa, Poisson’s ratio $\nu = 0.33$ and yield stress $\sigma_{ys0} = 276$ MPa. Similarly, $E = 113.8$ GPa, $\nu = 0.34$ and $\sigma_{ys0} = 880$ MPa for the titanium endcaps (ASM Handbook 1990; Boyer et al. 1994). We use the von Mises yield criterion

$$F = \sigma_{mises} - \sigma_{ys} \leq 0 \tag{3}$$

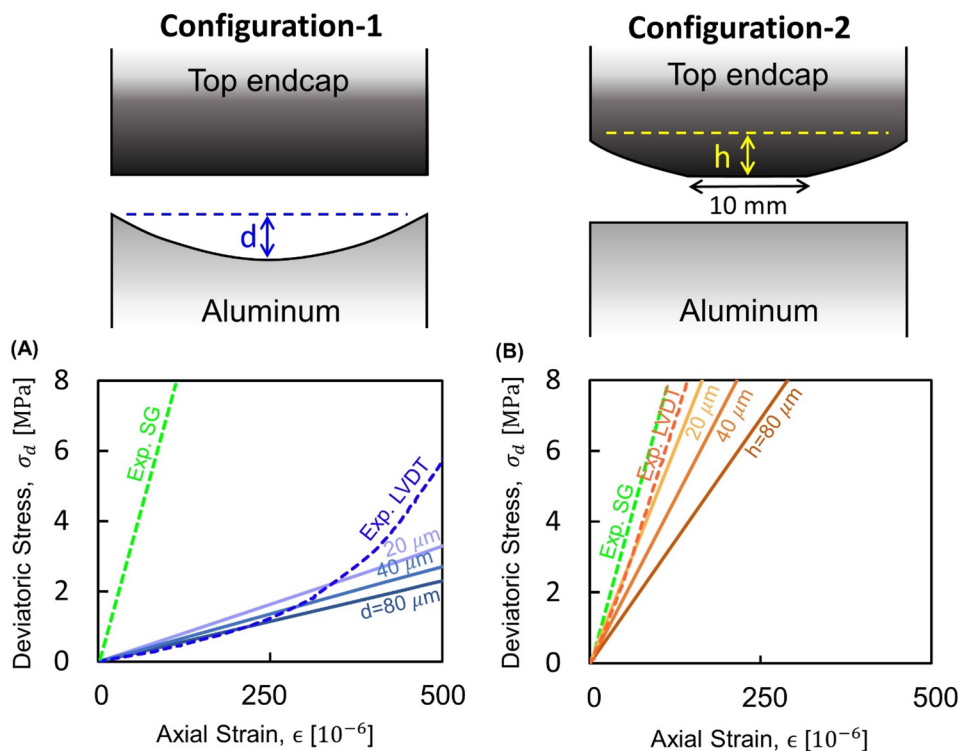
and isotropic linear hardening where the yield stress follows

$$\sigma_{ys} = \sigma_{ys0} + E_{iso} \epsilon_{pe} \tag{4}$$

$$E_{iso} = \frac{1}{\left(\frac{1}{E_{Tiso}} - \frac{1}{E} \right)} \tag{5}$$

where ϵ_{pe} is the effective plastic strain, E_{iso} the isotropic elastic modulus and E_{Tiso} the post-yield tangential modulus; for aluminum: $E_{Tiso} = 562$ MPa (Thota et al. 2015); titanium: $E_{Tiso} = 1.25$ GPa (Ziaja 2009). We

Fig. 9 Numerical and experimental stress–strain curves for the aluminum specimen. **a** Configuration-1: flat or polished endcaps on top of an aluminum specimen with a convex surface; the depth of convexity varies between $d = 20$ and $80 \mu\text{m}$. **b** Configuration-2: flat or polished aluminum specimen below concave-shaped endcaps; the height of concavity varies between $h = 20$ and $80 \mu\text{m}$. Green dashed line: experimental results from specimen-bonded strain gauges. Blue and orange dashed lines: cap-to-cap LVDT measurements. Continuous lines: numerical results



simulate two interface macro-topographies inspired by the measured surfaces (Fig. 9): (1) convex-aluminum surface on flat endcaps, and (2) concave endcaps against a flat aluminum surface (the flattened circular contact $d_{\text{contact}} = 10 \text{ mm}$ avoids numerical instability). Both of them are spherical sectors of radius R and height h . Simulations consider three different $[h, R]$ pairs: $[80 \text{ }\mu\text{m}, 1000 \text{ mm}]$, $[40 \text{ }\mu\text{m}, 2000 \text{ mm}]$, and $[20 \text{ }\mu\text{m}, 4000 \text{ mm}]$. Results in Fig. 9 show the seating effects on the stress–strain response computed from cap-to-cap deformation measurements. Clearly, convexity/concavity at interfaces has a pronounced effect on the inferred specimen response and its stiffness. Numerical results reveal a 29% decrease in estimated stiffness for 20 μm concavity height, reaching as much as 50% stiffness reduction for 80 μm concavity height. For comparison, experimental results show $\sim 8\%$ diminished elastic modulus for a measured concavity height of $\sim 14 \text{ }\mu\text{m}$.

4.2 Ultrasonic Velocity

Ultrasonic data gathered during the triaxial tests also show the effect of specimen-endcap interfaces by hindering energy transmission. We used the integral of the energy within a 10 μs time window and normalized the energy in a given signal by the energy in the signal gathered at 60 MPa. Figure 10 shows the normalized energy in P-wave signals as a function of deviatoric stress for both rough and polished aluminum specimens. The data reveal enhanced coupling and higher P-wave received energy at high axial stresses. In contrast, energy transmission drops by one (polished) to two (rough) orders of magnitude at lower deviatoric stress levels. Clearly, P-wave transmission emerges as a sensitive indicator of the evolving specimen-endcap interces.

We use coda wave analysis to accurately determine changes in first arrival times (Dai et al. 2013). The stretching

factor θ is proportional to the time shift of the first arrival time t between two signals a and b in a cascade:

$$\theta = \frac{\Delta t}{t_a} = \frac{(t_a - t_b)}{t_a} \tag{6}$$

Figure 11a and b display cascades of P- and S-wave signatures acquired for the polished aluminum specimen (a subset of the signals is shown for clarity). The red markers indicate first arrival times obtained from coda wave analysis where the signal at the highest deviatoric stress is used as the base trace. Figures 11c and d show the computed P- and S-wave velocities using the instantaneous specimen length, as a function of deviatoric stress during loading (red) and unloading (blue). While the transmitted acoustic energy changes with stress level (Fig. 10), coda wave analysis recovers changes in travel time even for low deviatoric stresses. The data show that propagation velocities increase with axial deviatoric stress following a Hertzian-type power function:

$$V = \alpha \left(\frac{\sigma_d}{1 \text{ MPa}} \right)^\beta \tag{7}$$

where α is the wave velocity at 1 MPa, and the β -exponent reflects the stress sensitivity. The low-stress sensitivity of wave velocity in aluminum $\beta = 0.003$ to 0.007 is caused by changes in interatomic distance. On the other hand, rock specimens tend to exhibit higher stress sensitivity than aluminum specimens due to inter-particle contact deformation (clastics), closure of micro-cracks and re-contact between debonded grains. Our measurement results show: Eagle Ford shale $\beta \sim 0.004$, Jubaila carbonate $\beta = 0.006$ to 0.013 , and Berea sandstone $\beta = 0.029$ to 0.032 (Fig. 12). In comparison, the stress sensitivity of the propagation velocity is much higher in fractured rocks and granular media where contact mechanics controls stiffness and the β -exponent can range from $\beta \approx 0.2$ to $\beta > 0.5$ (Cha et al. 2014).

Fig. 10 Transmitted P-wave energy as a function of deviatoric stress in polished and rough aluminum specimens—integral of the energy within the 10 μs time window (see inset) normalized by the energy measured at 60 MPa. Filled symbols correspond to the loading path while open symbols correspond to unloading

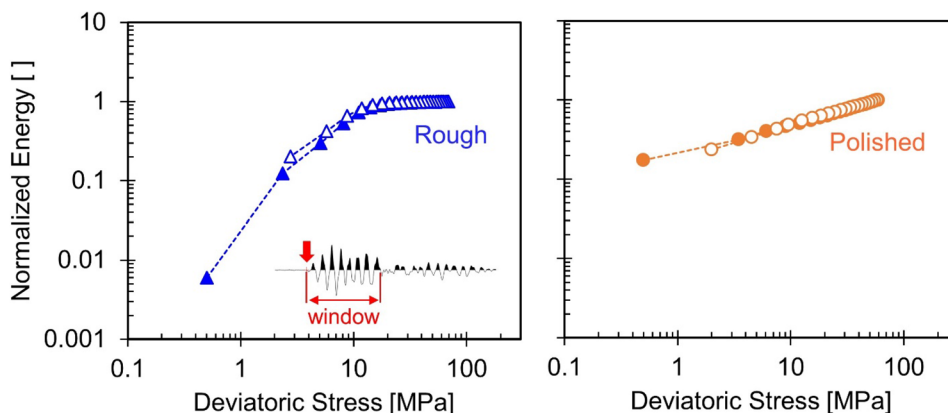


Fig. 11 Ultrasonic P- and S-wave data acquired with the polished aluminum specimen under unconfined conditions. Cascades of **a** P- and **b** S-wave signatures; red crosses indicate the first arrival times obtained through coda wave analysis. **c** and **d** Ultrasonic velocity as a function of deviatoric stress. Red points: loading. Blue points: unloading. P and S-wave velocities follow a Hertzian-type power function (Color figure online)

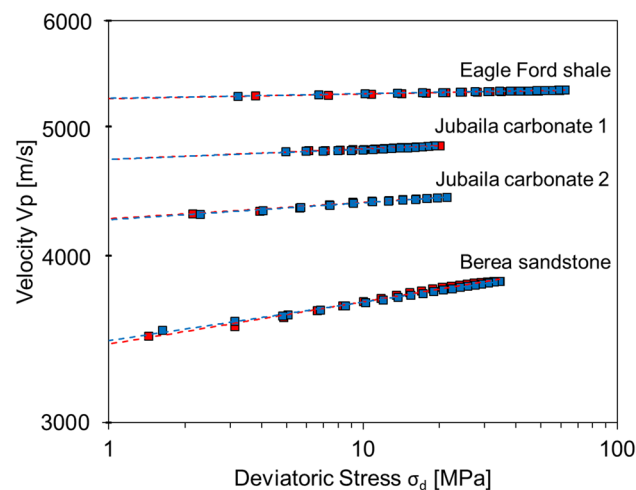
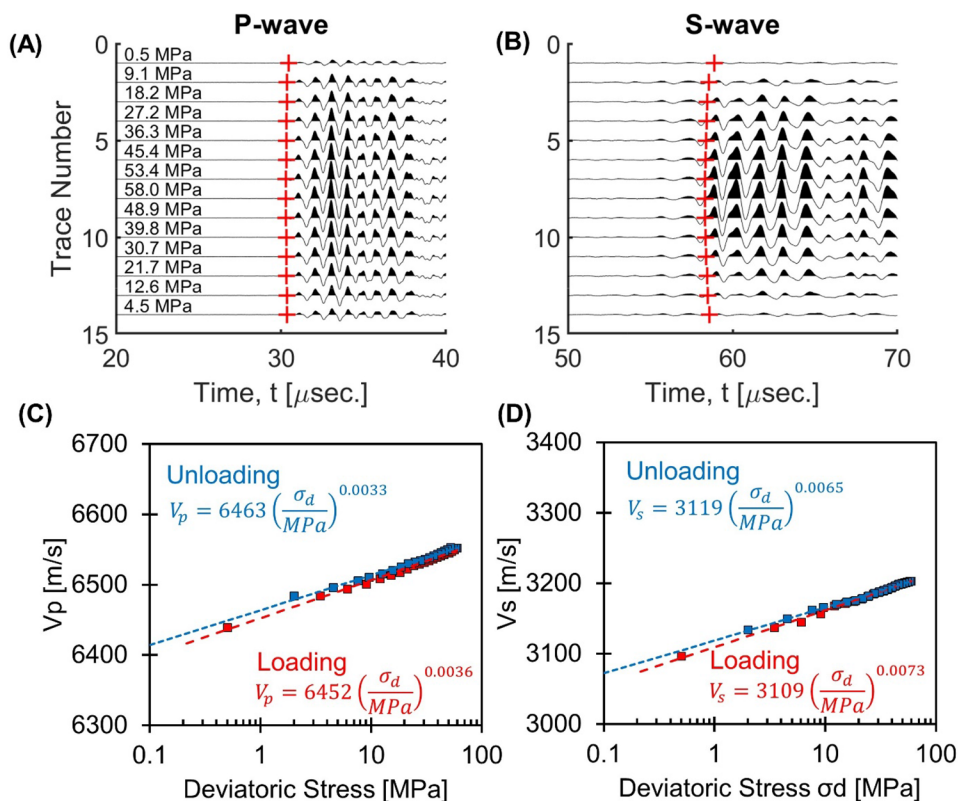


Fig. 12 P-wave velocity evolution during deviatoric loading: Berea sandstone, Eagle Ford shale, and Jubaila carbonates. The Berea sandstone displays the lowest α -factor and the highest β -exponent, which indicates lower velocity at low confinement yet higher stress sensitivity in comparison to other rock specimens. P-wave velocity trends are almost identical during loading (red) and unloading (blue) for the Eagle Ford shale and Jubaila carbonates. The small but consistent differences observed for Berea sandstone point to residual fabric changes after loading (Color figure online)

4.3 Impact on Static and Dynamic Moduli

The quasi-static modulus is a low-frequency measurement, where the wavelength is much longer than the specimen height $\lambda \gg L$, and the duration of the measurement is much longer than any internal time scale in the system $T_{\text{meas}} \gg T_{\text{int}}$. Typically, the static modulus is obtained from uniaxial compression stress–strain data (ASTM International D7012-14 (2014)). On the other hand, the dynamic modulus results from high-frequency measurements, and short wavelengths so that the perturbation may interact with internal time and spatial scales in the specimen (impulse response, ASTM International E (1876)-15 (2015); ultrasonic ASTM International E494-15 (2015); sonic resonance, ASTM International E (1875)-13 (2013); resonance column, ASTM International D4015-15e1 (2015); cyclic loading, ASTM International D5311/D5311M-13 (2013)). Table 4 summarizes test conditions for commonly used dynamic techniques.

The dynamic modulus obtained with high-frequency wave propagation is typically higher than the static modulus because of: (1) ballistic wave propagation along high velocity pathways that avoid low-velocity zones in heterogeneous media including grain debonding, and cavities (Zisman 1933; Ide 1936; Simmons and Brace 1965; Cheng 1981); (2) global-vs-local drainage conditions (Biot 1956; Dvorkin et al. 1995); and (3) strain level (Fjær 2019).

Table 4 Overview of dynamic measurement techniques to derive elastic moduli

Methods	Frequency range	Measurements	Excitation
Impulse response ASTM International E (1876)-15 (2015)	100 Hz–50 kHz (depends on specimen stiffness and size)	Fundamental resonant frequency	Mechanically by a singular elastic strike with an impulse tool
Ultrasonic ASTM International E494-15 (2015)	1–20 MHz	Pulse transit time	Low strain pulse using piezo transducers
Sonic resonance ASTM International E (1875)-13 (2013)	100–30,000 Hz	Resonant frequency	Variable-frequency audio oscillator. A speaker of the tweeter type or a magnetic cutting head
Resonance column ASTM International D4015-15e1 (2015)	0.1–300 Hz (for soils) (depends on specimen stiffness and size)	Fundamental resonant frequency	Flexural and longitudinal vibration using electromagnetic devices
Cyclic loading ASTM International D5311/D5311M-13 (2013)	0.1–2 Hz	Strain and phase shift	Loading–unloading using tri/uniaxial compression device

Fig. 13 Static and dynamic stiffness for the polished aluminum and Eagle Ford shale specimens at 0 MPa confining pressure. Black squares: dynamic modulus from wave propagation. Green squares: static modulus calculated from specimen-bonded strain gauges. Orange squares: static modulus from cap-to-cap LVDTs (Color figure online)

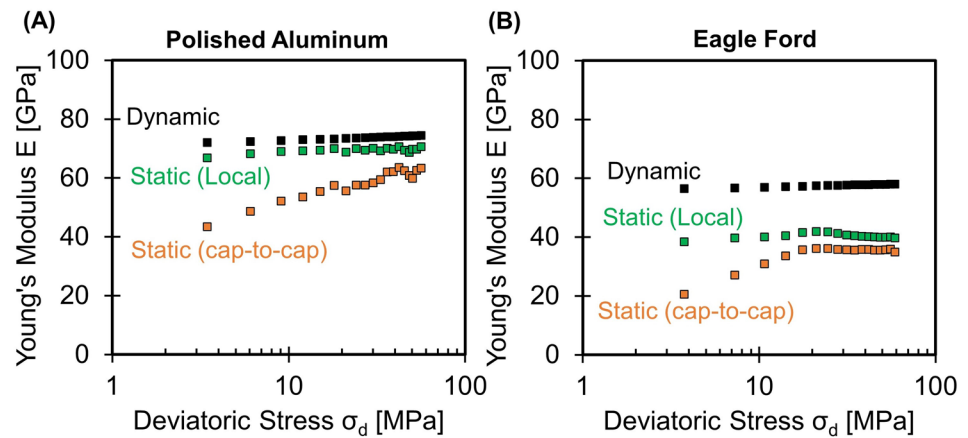


Figure 13 displays the static tangential modulus derived from strain gauge data (4 MPa deviatoric stress increment, strain level between 0.0005 and 0.0006), and the dynamic modulus computed from ultrasonic P- and S-wave velocities as a function of the deviatoric stress. Static and dynamic moduli follow the same loading trend with deviatoric stress σ_d , however, the dynamic modulus is higher than the quasi-static modulus, $E_{dyn}/E_{st} \geq 1$ in both the aluminum and shale specimen. For completeness, we include the static modulus estimated from cap-to-cap LVDTs deformation measurements: this static modulus is significantly lower and exhibits a markedly higher stress sensitivity due to the non-linear seating effects discussed above.

Figure 14 plots static E_{st} and dynamic E_{dyn} moduli compiled from the literature; the different symbols distinguish local and cap-to-cap instrumentations (empirical

relations for E_{dyn}/E_{st} can be found in King 1983; Eissa and Kazi 1988; Christaras et al. 1994; Brautigam et al., 1998; Mockovčhiaková and Pandula 2003; Soroush and Fahimifar 2003 and Brotons et al. 2014 and 2016). The figure includes values obtained as part of this research (Data shown at 15 MPa axial deviatoric stress only). Differences between dynamic and static moduli reduce when local strain measurements are used; in fact, previously reported E_{dyn}/E_{st} ratios are due in part to inherent measurement biases. However, the ratio remains $E_{dyn}/E_{st} \geq 1.0$ even when specimen-bonded strain gauges are used; therefore, internal spatial and time scales, strain level and propagation phenomena do affect the stiffness measured using wave propagation techniques.

Quasi-static strain rosette data and dynamic V_p/V_s measurements allow us to compute Poisson's ratios. The dynamic values are slightly higher than the static values in the tested shale and carbonate: $\nu_{dyn} = 0.27$ versus $\nu_{st} = 0.25$

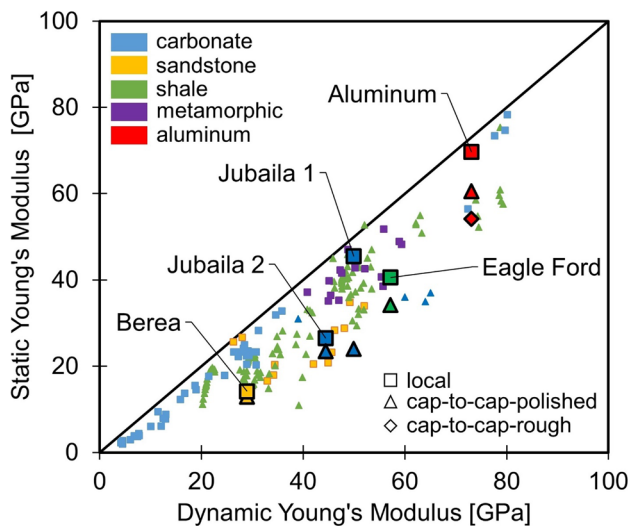


Fig. 14 Static versus dynamic Young's moduli. Colors: lithology or specimen type. Symbol shape: instrumentation (square = strain gauges; triangle = cap-to-cap polished specimens; diamond = cap-to-cap rough specimens). Large symbols show results gathered in this study at 15 MPa deviatoric stress. Small symbols correspond to published data for various rock types (Fei et al. 2016; Sone and Zoback 2013; Elkatatny et al. 2018; Gong et al. 2019; Mockovčičaková and Pandula 2003; Brotons et al. 2014, 2016)

for the Eagle Ford shale, and $\nu_{\text{dyn}} = 0.24$ versus $\nu_{\text{st}} = 0.21$ for the Jubaila carbonates.

4.4 Impact on Biot's α -Parameter

Biot's α -parameter relates the applied total stress σ and pore fluid pressure P_p to the effective stress σ' (Biot 1941),

$$\sigma' = \sigma - \alpha P_p \quad (8)$$

Biot's α -parameter requires careful measurement of the skeleton K_s and the grain K_m bulk moduli:

$$\alpha = 1 - \frac{K_s}{K_m} \quad (9)$$

Results presented above show that cap-to-cap LVDTs deformation measurements lead to a lower skeleton bulk modulus K_s due to seating effects which result in higher α -parameter values.

$$0 < \alpha_{\text{local}} < \alpha_{\text{global}} < 1 \quad (10)$$

While local strain measurements avoid the seating effects on stiffness, compliance effects at specimen-endcap interfaces still affect the pore pressure generation. Therefore, accurate polishing of endcaps and specimen surfaces will play a critical role in the determination of the α -parameter.

5 Conclusions

1. Surface roughness at the specimen-endcap interfaces causes high local deformation, tilting and even specimen bending. These seating effects affect the measurement of all mechanical properties, from stiffness and Poisson's ratio to Biot's poroelastic α -parameter. Seating effects are most pronounced at low normal stresses (relative to the specimen stiffness), that is, during the early stages of confinement and deviatoric loading.
2. Cap-to-cap LVDTs deformation measurements are particularly affected by seating effects. The measured stress-strain trends reflect significantly reduced stiffness and exhibit hysteresis. Measurement errors do not cancel when considering the average of diametrically opposite LVDT deformation measurements. The installation of deformation transducers over sleeve faces compliance issues and biases measurements.
3. Local strain measurements using specimen bonded strain gauges avoid seating effects and most of its consequences. Sealing is critical and prone to leakage in standard triaxial configurations. Mounting strain gauges on sleeves is ill-advised due to compliance effects.
4. Proper surface polishing limits the impact of seating effects. Polishing the specimen and endcaps may be important even when using specimen-bonded strain gauges. For example, compliance at the specimen-endcap interfaces affects pore pressure generation and the determination of Biot's α -parameter.
5. High-resolution profilometry measurements of specimen surfaces and triaxial endcaps provide a direct assessment of the topography and its potential impact on triaxial test data. Small spot-size profilometer data identifies differences in surface roughness often missed with the large mechanical tips currently used in standard testing protocols.
6. Surface roughness and the mismatch at specimen-endcap interfaces reduce the transmitted ultrasonic energy. Whilst this does not affect ultrasonic first arrivals per se, low energy transmission may impact the identification of first arrivals and affect the computed modulus.
7. Accurate measurements of deformation and strain in triaxial tests allow the study of important rock phenomena, such as differences between dynamic and static moduli, and the stress sensitivity of the dynamic modulus observed even in intact rock specimens.

Acknowledgements Support provided by the KAUST Endowment at King Abdullah University of Science and Technology for this research. Gabrielle E. Abelskamp edited the manuscript.

Open Access This article is licensed under a Creative Commons Attribution 4.0 International License, which permits use, sharing, adaptation, distribution and reproduction in any medium or format, as long as you give appropriate credit to the original author(s) and the source, provide a link to the Creative Commons licence, and indicate if changes were made. The images or other third party material in this article are included in the article's Creative Commons licence, unless indicated otherwise in a credit line to the material. If material is not included in the article's Creative Commons licence and your intended use is not permitted by statutory regulation or exceeds the permitted use, you will need to obtain permission directly from the copyright holder. To view a copy of this licence, visit <http://creativecommons.org/licenses/by/4.0/>.

References

- ASM Handbook (1990) Properties and selection: nonferrous alloys and special-purpose materials, 10th edn. ASM International, Materials Park, West Conshohocken, p 1300
- ASTM International D4015–15e1 (2015) Standard test methods for modulus and damping of soils by fixed-base resonant column devices. ASTM, West Conshohocken. <https://doi.org/10.1520/D4015-15E01>
- ASTM International D4543-08 (2008) Standard practices for preparing rock core as cylindrical test specimens and verifying conformance to dimensional and shape tolerances. ASTM, West Conshohocken. <https://doi.org/10.1520/D4543-08>
- ASTM International D5311/D5311M-13 (2013M) Standard test method for load controlled cyclic triaxial strength of soil. ASTM, West Conshohocken. https://doi.org/10.1520/D5311_D5311M-13
- ASTM International D7012-14 (2014) Standard test methods for compressive strength and elastic moduli of intact rock core specimens under varying states of stress and temperatures. ASTM, West Conshohocken. <https://doi.org/10.1520/D7012-14>
- ASTM International E1875-13 (2013) Standard test method for dynamic young's modulus, shear modulus, and poisson's ratio by sonic resonance. ASTM, West Conshohocken
- ASTM International E1876-15 (2015) Standard test method for dynamic young's modulus, shear modulus, and poisson's ratio by impulse excitation of vibration. ASTM, West Conshohocken. <https://doi.org/10.1520/E1876-15>
- ASTM International E494–15 (2015) Standard practice for measuring ultrasonic velocity in materials. ASTM, West Conshohocken. <https://doi.org/10.1520/E0494-15>
- Atkinson JH (2000) Non-linear soil stiffness in routine design. *Géotechnique* 50(5):487–508
- Baldi G, Hight DW, Thomas GE (1988) State-of-the-art Paper: a Reevaluation of Conventional Triaxial Test Methods. In: Donaghe RT, Chaney RC, Silver ML (eds) *Advanced Triaxial Testing of Soil and Rock*. ASTM STP 97, Philadelphia, pp 219–263
- Bhandari A, Powrie W, Harkness R (2012) A digital image-based deformation measurement system for triaxial tests. *ASTM Geotech Test J* 35(2):209–226
- Biot MA (1941) General theory of three-dimensional consolidation. *J Appl Phys* 12(2):155–164. <https://doi.org/10.1063/1.1712886>
- Biot MA (1956) Theory of propagation of elastic waves in a fluid-saturated porous solid. I. Low-frequency range. *J Acoust Soc Am* 28(2):168–178
- Boyer R, Welsch G, Collings EW (1994) *Materials properties handbook: titanium alloys*. ASM International, Materials Park
- Brautigam T, Knochel A, Lehne M (1998) Prognosis of uniaxial compressive strength and stiffness of rocks based on point load and ultrasonic tests. *Otto-Graf-J* 9:61–79
- Brotos V, Tomas R, Ivorra S (2014) Grediaga A (2014) Relationship between static and dynamic elastic modulus of calcarenite heated at different temperatures: the San Julia'n's stone. *Bull Eng Geol Environ* 73:791–799. <https://doi.org/10.1007/s10064-014-0583-y>
- Brotos V, Tomas R, Ivorra S, Grediaga A, Martinez MJ, Benavente D, Gomez-Heras M (2016) Improved correlation between the static and dynamic elastic modulus of different types of rocks. *Mater Struct* 49:3021–3037
- Cha M, Santamarina JC, Kim H, Cho G (2014) Small-strain stiffness, shear-wave velocity, and soil compressibility. *J Geotech Geoenviron Eng* 140(10):060140114
- Cheng CH (1981) Dynamic and static moduli. *Geophys Res Lett* 8(1):39–42
- Christaras B, Auger F, Mosse E (1994) Determination of the moduli of elasticity of rocks. Comparison of the ultrasonic velocity and mechanical resonance frequency methods with direct static methods. *Mater Struct* 27:222–228
- Clayton CRI, Khatrush SA (1986) A new device for measuring local axial strains on triaxial specimens. *Geotechnique* 36(4):593–597
- Dai S, Wuttke F, Santamarina JC (2013) Coda wave analysis to monitor processes in soils. *J Geotechn Geoenviron Eng* 139(9):1504–1511
- Dvorkin J, Mavko G, Nur A (1995) Squirt flow in fully saturated rocks. *Geophysics* 60(1):97–107
- Eissa EA, Kazi A (1988) Relation between static and dynamic Young's moduli of rocks. *Int J Rock Mech Min Sci Geomech Abstr* 25(6):479–482
- Elkatatny A, Mahmoud M, Mohamed I, Abdurraheem A (2018) Development of a new correlation to determine the static Young's modulus. *J Pet Explor Prod Technol* 8:17–30. <https://doi.org/10.1007/s13202-017-0316-4>
- Fei W, Huiyuan G, Jun Y, Yonghao Z (2016) Correlation of dynamic and static elastic parameters of rock. *Electron J Geotech Eng* 21(4):1551–1560
- Filho LMC (1985) Measurement of axial strains in triaxial tests on London Clay. *Geotech Test J* 8(1):3–13. <https://doi.org/10.1520/GTJ10851J>
- Fjær E (2019) Relations between static and dynamic moduli of sedimentary rocks. *Geophys Prospect* 67:128–139
- Gong F, Di B, Wei J, Ding P, Tian H, Han J (2019) A study of the anisotropic static and dynamic elastic properties of transversely isotropic rocks. *Geophysics* 84(6):C281–C293
- Hird CC, Yung PCY (1989) Use of proximity transducers for local strain measurements in triaxial tests. *Geotech Test J* 12(4):292–296
- Howarth DF (1984) Apparatus to determine static and dynamic elastic moduli. *Tech Note Rock Mech Rock Eng* 17:255–264
- Ide JM (1936) Comparison of statically and dynamically determined Young's modulus of rocks. *Proc Natl Acad Sci* 22:81–92
- Isah BW, Mohamad H, Harahap ISH (2018) Measurement of small-strain stiffness of soil in a triaxial setup, review of local instrumentation. *Int J Adv Appl Scia* 5(7):15–26. <https://doi.org/10.21833/ijaas.2018.07.003>
- Jardine RJ, Symes NJ, Burland JB (1984) The Measurements of soil stiffness in the triaxial apparatus. *Geotechnique* 34(3):323–340
- King MS (1983) Static and dynamic elastic properties of rocks from the Canadian shield. *Tech Note Int J Rock Mech Min Sci Geomech* 20(5):237–241. [https://doi.org/10.1016/0148-9062\(84\)90037-8](https://doi.org/10.1016/0148-9062(84)90037-8)
- Kumar SS, Khrisna AM, Dey A (2016) Local strain measurements in triaxial tests using on Sample transducers. *Indian Geotechnical Conference IGC2016*, pp 1–4
- Kung GTC (2007) Equipment and testing procedures for small strain triaxial tests. *J Chin Inst Eng Series A Chung-Kuo Kung Ch'eng*

- Hsueh K'an 30(4):579–591. <https://doi.org/10.1080/02533839.2007.9671287>
- Li L, Zhang X, Chen G, Lytton R (2016) Measuring unsaturated soil deformations during triaxial testing using a photogrammetry-based method. *Can Geotech J* 53(3):472–489. <https://doi.org/10.1046/j.1365-2850.2000.00333>
- Mockovčhiaková A, Pandula B (2003) Study of the relation between the static and dynamic moduli of rocks. *Metalurgija* 42(1):37–39
- Simmons G, Brace WF (1965) Comparison of static and dynamic measurements of compressibility of rocks. *J Geophys Res* 70(22):5649–5656. <https://doi.org/10.1029/JZ070i022p05649>
- Sone H, Zoback MD (2013) Mechanical properties of shale-gas reservoir rocks-part 1: Static and dynamic elastic properties and anisotropy. *Geophysics* 78(5):D381–D392
- Soroush H, Fahimifar A (2003) Evaluation of some physical and mechanical properties of rocks using ultrasonic pulse technique and presenting equations between dynamic and static elastic constants. *ISRM 2003–Technology roadmap for rock mechanics*, pp 1113–1118
- Symes M, Burland J (1984) Determination of local displacements on soil samples. *Geotech Test J* 7(2):49. <https://doi.org/10.1520/GTJ10593J>
- Tatsuoka F (1988) Some recent developments in triaxial testing systems for cohesionless soils. In: Donaghe RT, Chaney RC, Silver ML (eds) *Advanced triaxial testing of soil and rock*. ASTM, West Conshohocken, pp 7–67
- Thota J, Trabia M, O'Toole B (2015) Computational prediction of low impact shock propagation in a lab-scale space bolted frame structure. *Int J Comput Methods Eng Sci Mech* 3(2):139–149
- Tisato N, Madonna C (2012) Attenuation at low seismic frequencies in partially saturated rocks: measurements and description of a new apparatus. *J Appl Geophys* 86:44–53. <https://doi.org/10.1016/j.jappgeo.2012.07.008>
- van Heerden WL (1987) General relations between static and dynamic moduli of rocks. *Int J Rock Mech Min Sci Geomech* 24(6):381–385. [https://doi.org/10.1016/0148-9062\(87\)92262-5](https://doi.org/10.1016/0148-9062(87)92262-5)
- Wild KM, Barla M, Turinetti G, Amann F (2017) A multi-stage triaxial testing procedure for low permeable geomaterials applied to Opalinus Clay. *J Rock Mech Geotech Eng* 9(3):519–530
- Xu DS (2017) A new measurement approach for small deformations of soil specimens using fiber bragg grating sensors. *Sensors* 17(1016):1–13. <https://doi.org/10.3390/s17051016>
- Xu DS, Borana L, Yin JH (2014) Measurement of small strain behavior of a local soil by fiber Bragg grating-based local displacement transducers. *Acta Geotech* 9(6):935–943. <https://doi.org/10.1007/s11440-013-0267-y>
- Yimsiri S, Soga K, Chandler SG (2005) Cantilever-type local deformation transducer for local axial strain measurement in triaxial test. *Geotech Test J* 28(5):445–451. <https://doi.org/10.1520/GTJ11432>
- Ziaja W (2009) Finite element modelling of the fracture behaviour of surface treated Ti-6Al-4V alloy. *Assoc Comput Mater Sci Surf Eng* 1(1):53–60
- Zisman WA (1933) Comparison of the statically and seismologically determined elastic constants of rocks. *Proc National Acad Sci* 19:680–686

Publisher's Note Springer Nature remains neutral with regard to jurisdictional claims in published maps and institutional affiliations.